# Reconstructing the fluid flow by tracking of large particles

Francesco Romanò*

*Dept. Biomed. Eng., University of Michigan,*

*2123 Carl A. Gerstacker Building, 2200 Bonisteel Boulevard,*

*Ann Arbor, MI 48109-2099, USA and*

*Univ. Lille, CNRS, ONERA, Arts et Metiers ParisTech,*

*Centrale Lille, FRE 2017-LMFL-Laboratoire de Mécanique des*

*Fluides de Lille - Kampé de Fériet, F-59000, Lille, France*

(Dated: September 26, 2019)

## Abstract

All the methods which estimate the unperturbed fluid flow velocity relying on particle suspensions address the same question: How can the fluid velocity be computed measuring the particles trajectory and/or their velocities? The tracking of a few large density-mismatched particles is here used to efficiently and accurately reconstruct the background fluid flow. Approximating the particulate phase space and taking the limit of vanishing Stokes number $\mathrm{St} \to 0$, we retrieve the background flow for three test cases: a shear flow near a wall, a rigid-body vortex, and a strained vortex. The major advantages and the potentials of this approach are discussed in the end, highlighting how to overcome the classic shortcomings of experimental measurements faced for near-boundaries particle tracking.

* Email: frromano@umich.edu

## I. INTRODUCTION

Particle-laden flows consist of a dispersed phase made of rigid particles immersed in a continuous fluid phase. The relevance of this class of multiphase flows is readily understood considering that several natural phenomena (e.g. debris flows, [1], or transport of red blood cells, [2]) and industrial applications (e.g. aerosol technology, [3], or combustion, [4]) involve particle suspensions over a very wide range of scales.

The understanding, prediction and control of particle-laden flows is best achieved knowing the background flow, i.e. the fluid flow in the absence of the particulate phase. This becomes even more important when dilute suspensions are considered, and the motion of the particles is strongly correlated to the background flow and weakly correlated to collective effects [5, 6]. Moreover, the reconstruction of the unperturbed flow field in presence of the particulate phase is the goal of measurement techniques such as particle image velocimetry (PIV and $\mu$PIV, [7]) and particle tracking velocimetry [8].

The motion of a particle immersed in a fluid flow depends on the velocity of the fluid, on the presence of boundaries (walls, free surfaces, other particles, see [9, 10]), and on particle parameters which relate the shape, density and size of the particle to characteristic lengths, densities and time scales of the background flow [11]. Apart from very theoretical cases, the particle trajectory differs from the pathline of a tracer initialized at the same location and with the same velocity. This concept is best highlighted by considering the motion of a particle in an incompressible two-dimensional steady flow. In fact, the particulate dynamical system is intrinsically dissipative, whereas the fluid flow is a Hamiltonian system, where the Hamiltonian coincides with the streamfunction. One major consequence is the particle dynamics can admit attractors and repellors, while a corresponding tracer cannot [12]. Such considerations further extend to time-periodic two-dimensional and steady three-dimensional fluid flows, which are the analogous of a piecewise Hamiltonian system with 1.5 degrees of freedom [13].

The characterization of the dynamical properties of the particulate system immersed in a turbulent fluid flow has been studied by [14–16] using a point-particle model based on the Maxey–Riley equation [17]. They showed that the particle inertia induces preferential concentrations for the particles, and the characterization of the statistical and dynamical properties of the particulate system can be done in terms of the particle size, the particle-to-

fluid density ratio and the properties of the background flow. More recent investigations have considered the effect of finite-size particles which interact with the smallest active scales of a turbulent flow (i.e. the Kolmogorov scale, see e.g. [18–23] for experimental and theoretical studies). In this case the particle motion and the fluid flow are strongly affected by their mutual interactions, and an explicit equation which models the particle dynamics is not available. Hence, several numerical methodologies with different degrees of approximation have been developed to take into account the coupling between the two phases (see e.g. [24, 25]), and in the recent years different approaches have been proposed to reconstruct the undisturbed fluid flow for two-way coupled Euler-Lagrangian simulation (see e.g. [26–29]). For a review of mixed particles in developed turbulence and of particle-modulated turbulent flows we refer to [30]. Particle suspensions are, however, also used in laminar flows and especially in microfluidics, and in such low-Reynolds-numbers flows the relevant flow scale cannot be identified by Kolmogorov scaling. Hence, in the followings, we will address as *large particles* all those particles whose size $a_\mathrm{p}$ (equivalent radius) is comparable to the length scale of the background flow $L$ which we want to reconstruct, i.e. $a_\mathrm{p} = \mathcal{O}(10^{-2} - 10^{0})L$.

An important parameter for particle-laden flows is the Stokes number, defined as $\mathrm{St} = 2\mathrm{Re}\rho_\mathrm{p} a_\mathrm{p}^2 / 9\rho_\mathrm{f} L^2$, where $\rho_\mathrm{p}$ and $\rho_\mathrm{f}$ are the density of the particle and of the fluid, respectively, $a_\mathrm{p}$ is the radius of the particle, $L$ the characteristic length scale of the fluid flow, $\mathrm{Re} = UL/\nu$ is the Reynolds number of the unperturbed flow and $\nu$ the kinematic viscosity of the fluid. The limit for $\mathrm{St} \to 0$ leads the particle to behave like a tracer, hence the particle velocity becomes a direct measure of the background fluid flow. Following the classic experimental approach, i.e. employing smaller and smaller particles (better if density matched to the fluid), has major experimental shortcomings. In fact, there are technological limitations in accurately tracking very small particles, and the smaller the particle, the harder and inaccurate the tracking. Thereafter, particle–boundary interactions strongly influence the particle trajectories at distance $\mathcal{O}(a_\mathrm{p})$ from the boundary [31, 32]. As a result, near a wall or a free surface, the particle velocity remarkably deviates from the velocity of the fluid. Moreover, even for conditions in which almost-tracer particles can be accurately tracked, employing very small particles requires a very expensive experimental apparatus.

In this paper, we propose to exploit the dissipative effects related to the particle finite size and the particle-to-fluid density and velocity mismatch in order to efficiently reconstruct the background flow. Rather than following the approach $\mathrm{St} \approx 0$ by employing smaller and

smaller particles with the same Stokes number, we reconstruct the particle phase space for finite-size (even relatively large) particles with different Stokes numbers and then compute the limit for $\mathrm{St} \to 0$ in the approximated phase space, constraining $\rho_\mathrm{p}/\rho_\mathrm{f}$ to remain finite and not tend to zero. For three cases, it will be shown that very accurate estimates of the fluid flow velocity can be obtained, and that the difficulties of estimating the fluid flow velocity near the boundaries can be overcome.

Recalling that the Maxey–Riley equation has been used by [33] to study the effect of the Faxén correction for finite-size particles in turbulent flows, we will employ this same particle motion model to theoretically demonstrate the potential of our approach. The concept at the basis of our study is however not limited by the use of the Maxey–Riley equation, since the methodology we propose does not rely on it. Assuming the Maxey–Riley equation as particle motion model, the fluid flow velocity could be computed by solving an inverse problem in which the particle trajectory is given and the fluid velocity is unknown. We stress, however, that this is not the purpose of our paper and the Maxey–Riley equation is employed just for demonstration purpose. The aim of this study is to propose an approach to reconstruct the background flow regardless of how the particle trajectories are numerically or experimentally obtained. By only exploiting the tracer limit, our paper will demonstrate how to reliably and accurately retrieve the background flow by approximating the phase space and taking the limit $\mathrm{St} \to 0$. The only requirement of our approach is the assumption that there are no phase-space catastrophes, i.e. the phase space subdomain employed in the neighborhood of $\mathrm{St} = 0$ to compute the limit $\mathrm{St} \to 0$ must be smooth enough. This is not the case for *caustics*, i.e. singularities in the particle dynamics which imply that the phase space manifold of the particulate flow admits a fold [34]. Hence, the approach proposed in this study is limited, in general, to $\mathrm{St} < \mathcal{O}(1)$.

The remainder of this paper is structured as follows: Sec. II defines the mathematical model, which is solved numerically as described in Sec. III. Section IV reports the results of our study for the three flows considered and discusses them. The conclusions are drawn in Sec. V, pointing out the potentials of the current approach.

## II. PROBLEM FORMULATION

The motion of a rigid spherical particle in an incompressible flow is modeled by a modified version of the Maxey–Riley equation [17], in which we include the force exerted by the boundaries on the particle

$$\rho_{\mathrm{p}}\frac{\mathrm{d}\boldsymbol{v}}{\mathrm{d}t}=\rho_{\mathrm{f}}\frac{\mathrm{D}\boldsymbol{u}}{\mathrm{D}t}+(\rho_{\mathrm{p}}-\rho_{\mathrm{f}})\,\boldsymbol{g}-\frac{9\nu\rho_{\mathrm{f}}}{2a_{\mathrm{p}}^2}\left(\boldsymbol{v}-\boldsymbol{u}-\frac{a_{\mathrm{p}}^2}{6}\nabla^2\boldsymbol{u}\right)-\frac{\rho_{\mathrm{f}}}{2}\left[\frac{\mathrm{d}\boldsymbol{v}}{\mathrm{d}t}-\frac{\mathrm{D}}{\mathrm{D}t}\left(\boldsymbol{u}+\frac{a_{\mathrm{p}}^2}{10}\nabla^2\boldsymbol{u}\right)\right]$$
$$+\boldsymbol{F}_b-\frac{9\rho_{\mathrm{f}}}{2a_{\mathrm{p}}}\sqrt{\frac{\nu}{\pi}}\int_0^t\frac{1}{\sqrt{t-\tau}}\frac{\mathrm{d}}{\mathrm{d}\tau}\left(\boldsymbol{v}-\boldsymbol{u}-\frac{a_{\mathrm{p}}^2}{6}\nabla^2\boldsymbol{u}\right)\mathrm{d}\tau, \tag{1}$$

where $t$ is the time, $\boldsymbol{v}=(v_x,v_y)$ and $\boldsymbol{u}=(u_x,u_y)$ denote the velocity of the particle and of the fluid, respectively, and $\boldsymbol{g}$ indicates the gravity acceleration. The rate of change of the particle momentum is represented by the left-hand side of (1), whereas the right-hand side includes: the force due to the background flow, the buoyancy term, the Stokes drag, the added mass, the particle–boundary interaction force $\boldsymbol{F}_b$, and the Basset history force. In addition, the Faxén correction [35] is taken into account by the terms proportional to $a_{\mathrm{p}}\nabla^2\boldsymbol{u}$. The effect of the particle rotation is neglected. The different notations used for indicating the material derivatives $\mathrm{d}_t$ and $\mathrm{D}_t$ refer to the derivative along the particle trajectory

$$\frac{\mathrm{d}\boldsymbol{A}}{\mathrm{d}t}=\frac{\partial\boldsymbol{A}}{\partial t}+(\boldsymbol{v}\cdot\nabla)\,\boldsymbol{A} \tag{2}$$

and along the fluid trajectory

$$\frac{\mathrm{D}\boldsymbol{A}}{\mathrm{D}t}=\frac{\partial\boldsymbol{A}}{\partial t}+(\boldsymbol{u}\cdot\nabla)\,\boldsymbol{A}, \tag{3}$$

where $\boldsymbol{A}$ denotes an arbitrary vector field and $\partial_t$ is the Eulerian derivative.

The interaction between a particle and a rigid wall is modeled assuming that, near the boundary, the particle is immersed in a creeping flow. Such an assumption holds true if the particle Reynolds number, $\mathrm{Re}_{\mathrm{p}}=|\boldsymbol{u}-\boldsymbol{v}|a_{\mathrm{p}}/\nu\ll 1$, where $\boldsymbol{u}$ and $\boldsymbol{v}$ denote the dimensional fluid flow and particle velocity evaluated at the particle centroid. If we further consider $|\boldsymbol{u}-\boldsymbol{v}|a_{\mathrm{p}}^2/\nu h$, where $h$ is the distance of the particle centroid from the wall, the flow around the particle is governed by Stokesian dynamics. Hence, it is described by a linear momentum equation and different contributions to the particle–wall interaction can be

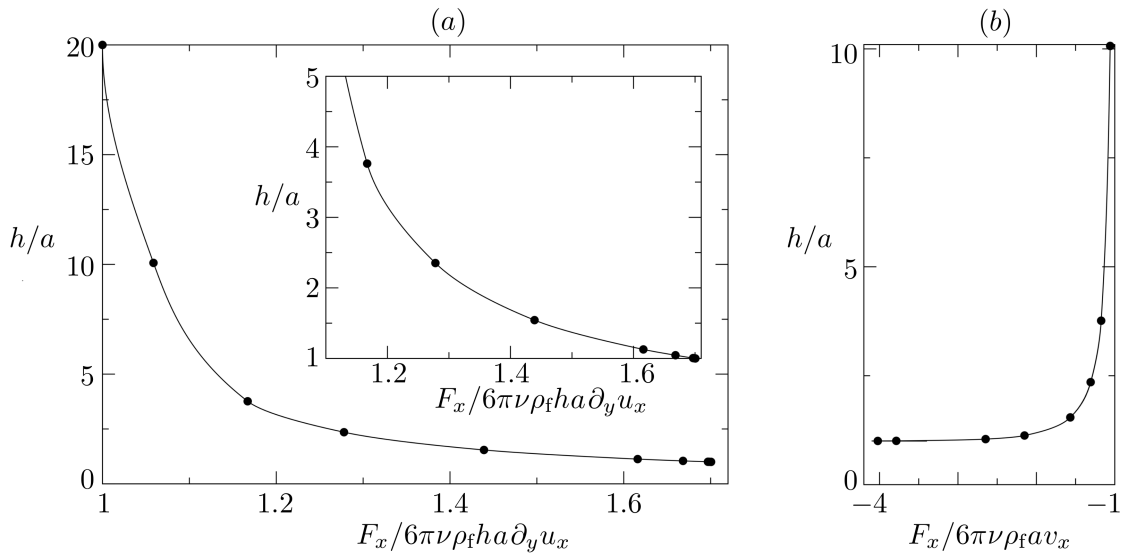


FIG. 1. (a) Force $F_x$ exerted by the fluid on a steady particle in a creeping shear flow near a steady wall. Bullets: solution of [37]; solid line: cubic spline interpolant of the results reported in tab. 1 of [37]. (a) Force $F_x$ exerted by the fluid on a particle moving in a quiescient flow near a steady wall. Bullets: solution of [38]; solid line: cubic spline interpolant of the results reported in tab. 1 of [38].

superposed splitting the problem in three sub-problems. The boundary force $\boldsymbol{F}_b = (F_x,\ F_y)$ is computed by superposing: (a) the force on a particle moving towards a rigid wall, (b) the force on a steady particle immersed in a near-wall shear flow, and (c) the force on a particle moving along a solid wall. For consistency with (1), the effect of the particle rotation is neglected.

Case (a) gives rise to $F_y$, and an exact solution is reported in [36]

$$\frac{F_y}{6\pi\nu\rho_f a_p v_y} = \frac{4}{3}\sinh\alpha\sum_{n=1}^{\infty}\frac{n(n+1)}{(2n-1)(2n+3)}\left[\frac{2\sinh(2n+1)\alpha+(2n+1)\sinh(2\alpha)}{4\sinh^2(n+1/2)\alpha-(2n+1)^2\sinh^2\alpha}-1\right], \tag{4}$$

where $\alpha = \cosh^{-1}(h/a_p)$.

Cases (b) and (c) give rise to an $F_x$ obtained by superposing the approximated solutions by [37] and by [38] for case (b) and (c), respectively. Their results are here included in the Maxey–Riley equation by interpolating tab. 1 of [37] and tab. 1 of [38] by cubic splines. The result of the interpolations is depicted by solid lines in fig. 1, whereas the original data are denoted by the bullets.

## III. NUMERICAL SIMULATIONS

The Maxey–Riley equation is solved by means of the 4th-order Runge–Kutta, 3/8-rule. The Basset-history term is discretized explicitly following the same approach of [39], where the code has been validated. Throughout this paper, the time step is set equal to $\Delta t = 10^{-3}$ when dealing with unbounded flows, and $\Delta t = 10^{-5}$ for particle trajectories near a wall.

The data obtained by tracking the particles are scattered in the particulate phase space, hence, a meshless interpolant is required to numerically reconstruct a phase space approximation. The reconstruction of the particulate phase space is carried out by using a multiquadratic radial basis interpolant. The radial basis functions $\phi(r)$ have as argument the scalar radius $r = ||\boldsymbol{x} - \boldsymbol{x}_i||_2$ from the $i$-th coordinate to interpolate $\boldsymbol{x}_i$. We use a generalized radial basis function interpolant $f_{RBF}(\boldsymbol{x})$ for approximating the multivariate function $f(\boldsymbol{x})$. This yields

$$f_{RBF}(\boldsymbol{x}) = \sum_{l=1}^{L} \beta_l p_l(\boldsymbol{x}) + \sum_{n=1}^{N} \lambda_n \phi(||\boldsymbol{x} - \boldsymbol{x}_n||_2), \tag{5}$$

where $N$ is the number of nodes to interpolate, $p_l$ are the elements of a hierarchical polynomial functional basis usually employed to make the interpolant $f_{RBF}$ positive definite, and $L$ is the maximum order of the polynomials. The coefficients $\beta_l$ and $\lambda_n$ are found using the matching conditions $f_{RBF}(\boldsymbol{x}_i) = f(\boldsymbol{x}_i)$ and imposing the following homogenous conditions to constrain the interpolant: $\sum_{n=1}^{N} \lambda_n p_l(\boldsymbol{x}) = 0,\ 1 \leq l \leq L$. The multiquadratic functions are defined as $\phi(r) = \sqrt{1 + (r/\sigma)^2}$, where $\sigma$ is set equal to the average distance between the nodes. In our study, $L$ is set equal to 2.

## IV. RESULTS AND DISCUSSION

### A. Shear flow near a wall

The first case we consider is a linear shear flow near a rigid wall characterized by the length scale $H$, initial distance of the particle centroid from the rigid wall, and the velocity scale $U$, fluid flow velocity at distance $H$ from the wall. Scaling lengths, velocities and time by $H$, $U$ and $H/U$, the unperturbed fluid flow velocity is $\boldsymbol{u} = (y, 0)$ (see inset of fig. 2(a) and left panel of fig. 2(c)) and the non-dimensional Maxey–Riley equation for an initially

velocity-matched particle reads

$$\frac{\mathrm{d}\boldsymbol{v}}{\mathrm{d}t} = \frac{1}{\varrho + 1/2}\left[\frac{3}{2}\frac{\mathrm{D}\boldsymbol{u}}{\mathrm{D}t} - \frac{\varrho\lambda}{\mathrm{St}}(\boldsymbol{v}-\boldsymbol{u}) + \frac{(\varrho-1)}{\mathrm{Fr}^2}\boldsymbol{e}_g - \sqrt{\frac{9\varrho}{2\pi\mathrm{St}}}\int_0^t \frac{1}{\sqrt{t-\tau}}\frac{\mathrm{d}}{\mathrm{d}\tau}(\boldsymbol{v}-\boldsymbol{u})\,\mathrm{d}\tau\right], \quad (6)$$

where, $\boldsymbol{e}_g = \boldsymbol{g}/|\boldsymbol{g}| = (0,-1)$, $a = a_\mathrm{p}/H$ and $\boldsymbol{u}$, $\boldsymbol{v}$ and $t$ are now intended as non-dimensional velocities and time. Beside $\varrho$, St and Re, another non-dimensional group arises: the Froude number $\mathrm{Fr} = U/\sqrt{gH}$. In (6), the Faxén correction is identically null since $\nabla^2\boldsymbol{u} \equiv 0$ and the parameter $\lambda$ is used to take into account the boundary-induced forces on the particle due to its finite size. We assume that the particle dynamics near the wall is dominated by creeping flow effects and the corresponding enhanced particle drag is taken into account as explained in Sec. III. We further remark that no lift forces are included when considering the Stokesian solutions of [36–38].

The trajectory of five relatively large particles is computed by numerical integration of (6) and the Basset term is neglected in this first example. The fluid flow parameters are $\mathrm{Re} = 1$ and $\mathrm{Fr}^2 \in \{10^{-4}, 10^{-5}, 10^{-6}\}$, and the five particles have $(a,\varrho) = (0.02, 0.5)$, $(0.02, 2.5)$, $(0.03, 1.7)$, $(0.04, 0.8)$ and $(0.05, 1.05)$.

The smaller the Froude number, the larger the effect of gravity becomes, if compared to the shear flow velocity. Hence, for $\mathrm{Fr}^2 = 10^{-6}$ the particle trajectory is strongly affected by sedimentation effects and reconstructing the background flow using large-particle trajectories becomes very challenging. This is the case presented in fig. 2, where sedimenting particles travel a longitudinal distance which is 200 times smaller than the traveled height, as shown by the particle trajectories in fig. 2(a) and by the fast sedimentation velocity depicted in the bottom panel of fig. 2(b). Analogous results for the larger-Froude-number cases are reported in the Appendix.

The deviation between the velocity of the particle and the velocity of the fluid is depicted in fig. 2(b). The top panel shows the relative deviation in terms of horizontal velocity, the middle panel depicts the particle-to-fluid difference in $x$-velocity, and the bottom panel shows the vertical velocity of the particle (we recall that $u_y \equiv 0$). The major deviations are observed for particles which approach the boundary. Near the wall, the infinite-norm of their relative deviation between longitudinal velocities is about 60% (see $*$ and $\square$ in the top panel of fig. 2(b)). This makes very unreliable the near-boundary estimate of the fluid velocity based on the particle velocity. Moreover it demonstrates the limitations of reducing

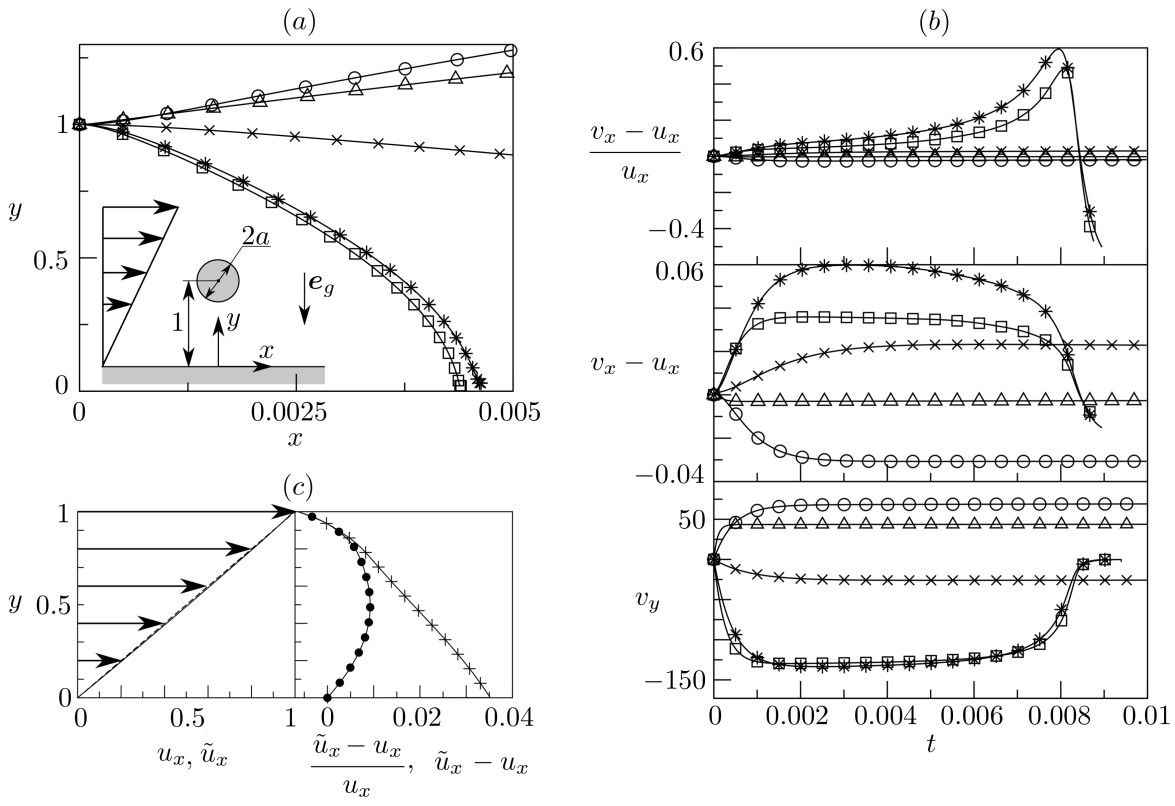


FIG. 2. (a) Particle trajectories and sketch of the background shear flow. (b) Deviation of the particle velocity from the fluid flow velocity. (c) Fluid flow velocity $u_x$ (arrows and dashed line), approximation of the fluid flow $\tilde{u}_x$ (solid line), relative (+) and absolute (•) approximation error (right panel) for the horizontal velocity. In (a) and (b), the markers depict: $(a, \varrho) = (0.02, 0.5)$, $\circ$, $(0.02, 2.5)$, $\square$, $(0.03, 1.7)$, $*$, $(0.04, 0.8)$, $\triangle$, and $(0.05, 1.05)$, $\times$. All the results refer to $\mathrm{Fr}^2 = 10^{-6}$.

the particle size for reconstructing near-boundary flows without taking the limit $\mathrm{St} \to 0$. Indeed, halving the Stokes number by passing from $a = 0.03$ $(*)$ to $a = 0.02$ $(\square)$ brings the infinite-norm of the relative deviation in longitudinal velocity from 59% only to 48%.

Instead of relying on the tracking of a single particle which might approximate the flow relatively well, we rather reconstruct the shear flow profile by approximation of the phase space of the particulate dynamical system. Gathering the trajectories and the velocities of all the five particles, we obtain a discrete characterization of $v_x$ in the hyperspace $(\mathrm{St}, \varrho, y)$, defined on scattered points. We then use multiquadratic radial basis functions to define an interpolant $V_x(\mathrm{St}, \varrho, y)$ which considers St, $\varrho$ and $y$ as coordinates and $v_x$ as function to interpolate. The boundary condition along the wall $v_x(\mathrm{St} \to 0, \varrho, y = 0) = u_x(y = 0) = 0$ is

finally enforced when constructing the interpolant $V_x$ by applying $V_x(St \to 0, \varrho, y = 0) = 0$. Computing the limit $\tilde{u}_x = \lim_{\mathrm{St}\to 0} V_x(\mathrm{St}, \varrho, y) \approx u_x(y)$ leads to an approximation of the fluid flow velocity $u_x$ (arrows and dashed line in the left panel of fig. 2(c)). Such an approximation is depicted as solid line in the left panel of fig. 2(c) for $\mathrm{Fr}^2 = 10^{-6}$. The right panel of fig. 2(c) shows the absolute and relative deviation of $\tilde{u}_x$ from $u_x$ as function of $y$. Respectively, they are at most about 1% and 4% even though only five particles have been used to approximate the particle parameter space. We remark that the relative deviation in terms of longitudinal velocity is one order of magnitude more accurate than what obtained by the single-particle tracking of the smallest particle we used (for $a = 0.02$ the relative deviation is 48%). The reconstruction of the shear flow becomes more accurate for $\mathrm{Fr}^2 = 10^{-5}$, for which $\tilde{u}_x - u_x$ and $(\tilde{u}_x - u_x)/u_x$ are, at most, 0.5% and 0.8%. Even better for $\mathrm{Fr}^2 = 10^{-4}$, where $\max(\tilde{u}_x - u_x)$ and $\max((\tilde{u}_x - u_x)/u_x)$ are 0.15% and 0.23%.

### B. Solid-body vortex

The second example we consider is a two-dimensional Kirchhoff vortex. In this case we include the Basset history force and neglect gravitational forces. Since the vortex is unbounded, $\boldsymbol{F}_b \equiv 0$. Lengths, velocities and time are scaled, respectively, by the characteristic radius $R$ of the vortical region to reconstruct, the characteristic velocity $\Omega R$, where $\Omega$ is the constant flow vorticity, and by the characteristic time scale $1/\Omega$. The non-dimensional velocity field is given by $\boldsymbol{u} = (u_x, u_y) = (y/2, -x/2)$ and the fluid flow Reynolds number is assumed to equal $\mathrm{Re} = \Omega R^2/\nu = 1$.

Only two particles are here employed to reconstruct the fluid flow: one particle lighter than the fluid $(a, \varrho) = (0.1, 0.8)$ is initialized at $(x, y) = (-0.5, 0)$, the other, much heavier than the fluid $(a, \varrho) = (0.2, 10)$, is initialized at $(x, y) = (0.5, 0)$. These particle parameters are chosen to exploit the inertial attraction/repulsion of the lighter/heavier particle to the steady vortex core. Especially when a remarkable density mismatch is employed, the particle experiences a pronounced spiraling motion which cannot be admitted by fluid elements. This would be a drawback in the classic experimental approach for measuring the flow velocity, but it is here exploited to let the particle acting like a probe by moving away from the initial streamline and reporting information about the fluid flow in a broad region of the fluid domain.

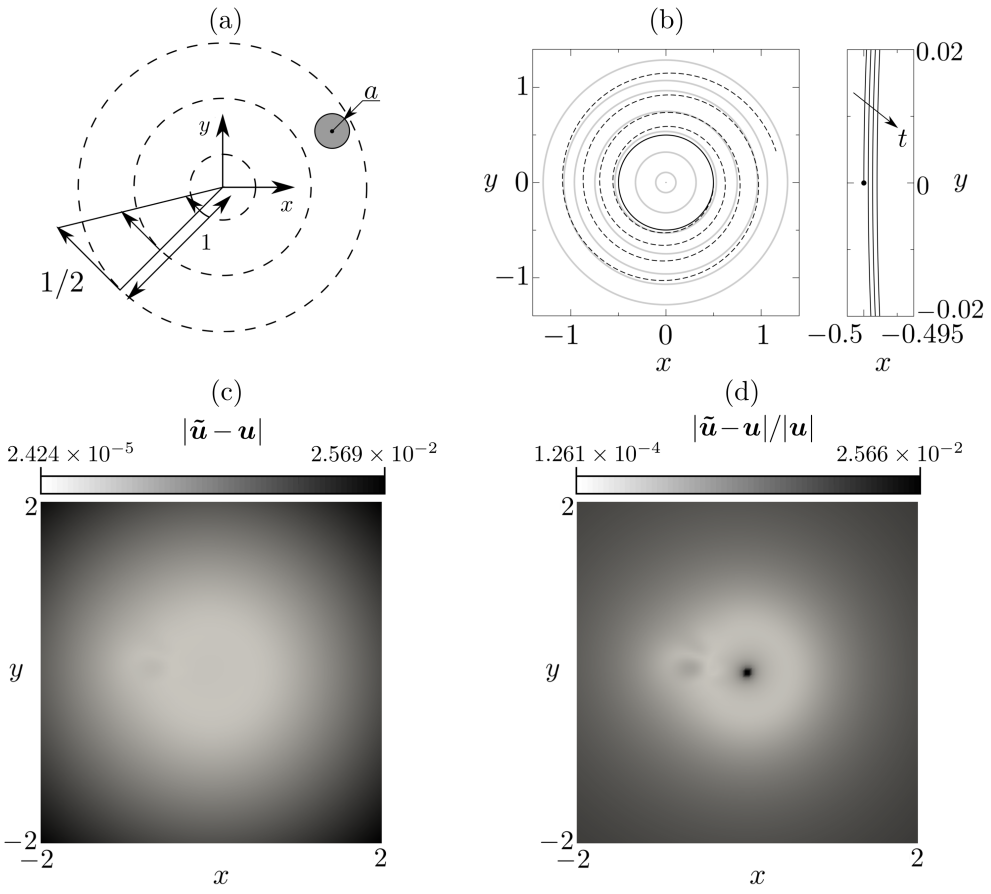


FIG. 3. (a) Sketch of the background Kirchhoff vortex. (b) Particle trajectories for $(a, \varrho) = (0.1, 0.8)$ and $(a, \varrho) = (0.2, 10)$ (solid and dashed line, respectively), and streamlines (gray). (c) Absolute approximation error, $|\tilde{\boldsymbol{u}} - \boldsymbol{u}|$. (d) Relative approximation error, $|\tilde{\boldsymbol{u}} - \boldsymbol{u}|/|\boldsymbol{u}|$.

A sketch of the fluid flow is reported in fig. 3(a); the spiraling-out (dashed line) and spiraling-in (solid line) trajectories of our two particles are depicted fig. 3(b), together with the flow streamlines (gray). Based on the two particle trajectories, the hyperspace in $(\mathrm{St}, \varrho, x, y)$ is approximated by the interpolant $\boldsymbol{V}(\mathrm{St}, \varrho, x, y)$, which is the analogous of $V_x$ introduced above for the shear flow near a wall. Once again, computing the limit $\tilde{\boldsymbol{u}} = \lim_{\mathrm{St}\to 0} \boldsymbol{V}(\mathrm{St}, \varrho, x, y) \approx \boldsymbol{u}(x, y)$ we construct an approximation of the fluid flow. Even if we challenge our approach making use of only two (relatively large) particles, the magnitude of the absolute ($|\tilde{\boldsymbol{u}} - \boldsymbol{u}|$, fig. 3(c)) and relative approximation error ($|\tilde{\boldsymbol{u}} - \boldsymbol{u}|/|\boldsymbol{u}|$, fig. 3(d)) are always below 2.5%.

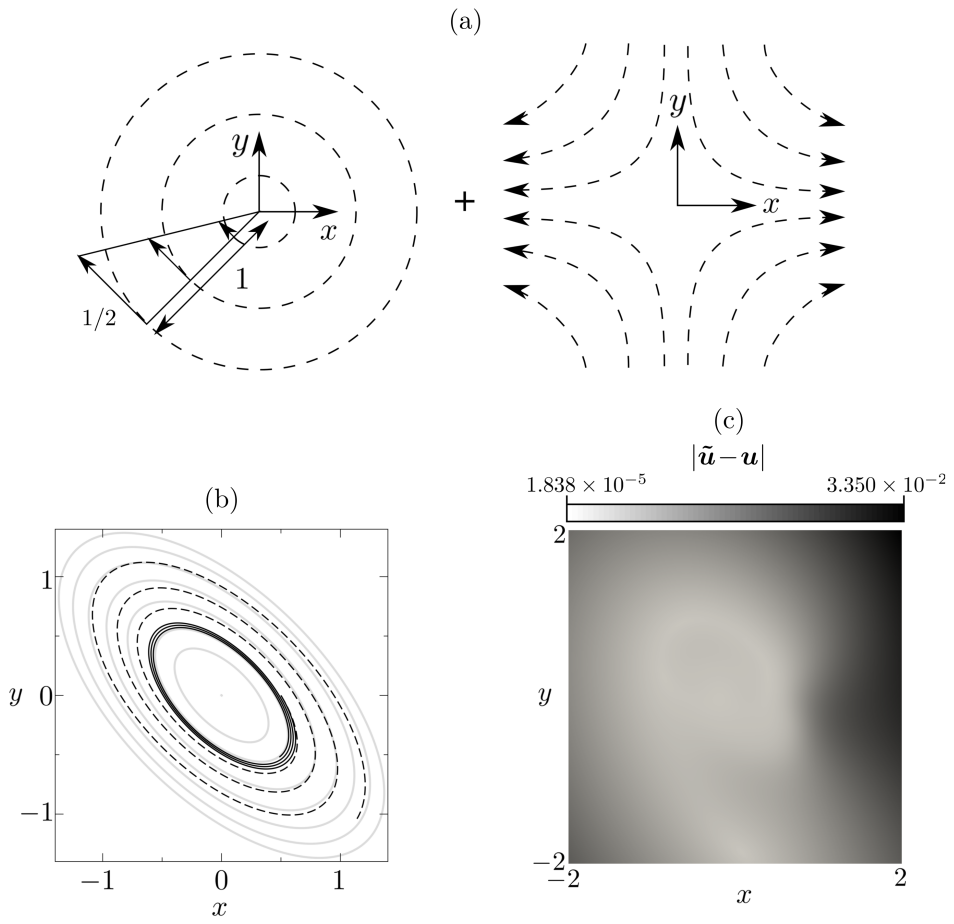


FIG. 4. (a) Sketch of the background strained vortex. (b) Particle trajectories for $(a, \varrho) = (0.5, 0.7)$ and $(a, \varrho) = (0.3, 6)$ (solid and dashed line, respectively), and streamlines (gray). (c) Absolute approximation error, $|\tilde{\boldsymbol{u}} - \boldsymbol{u}|$.

### C. Strained vortex

So far, only pure shear flows have been reconstructed by approximation of the particulate phase space. The last test case introduces a strain component, which is superposed to a Kirchhoff vortex leading to the fluid velocity $\boldsymbol{u} = (u_x, u_y) = (y/2 + 0.3x, -x/2 - 0.3y)$, see fig. 4(a). Two very large particles are initialized velocity-matched to the fluid flow at $(x, y) = (0.5, 0)$: one of them lighter than the fluid $(a, \varrho) = (0.5, 0.7)$, the other one heavier $(a, \varrho) = (0.3, 6)$. Their trajectories are reported in fig. 4(b) using solid and dashed line, respectively. The background flow streamlines are depicted by gray contours. Making use of the two particle trajectories, the hyperspace in $(\mathrm{St}, \varrho, x, y)$ is interpolated with multiquadratic radial

basis functions leading to $\boldsymbol{V}(\mathrm{St}, \varrho, x, y)$. The reconstruction of the fluid flow is carried out by taking the limit $\tilde{\boldsymbol{u}} = \lim_{\mathrm{St}\to 0} \boldsymbol{V}(\mathrm{St}, \varrho, x, y) \approx \boldsymbol{u}(x, y)$. Even if the tracked particles remarkably deviate from the conceptual limit of perfect tracers, our reconstruction of the fluid flow deviates from the actual background flow of, at most, 3.5% in relative ($|\tilde{\boldsymbol{u}} - \boldsymbol{u}|/|\boldsymbol{u}|$, not shown) and absolute error ($|\tilde{\boldsymbol{u}} - \boldsymbol{u}|$, fig. 4(c)).

## V. CONCLUSION

Tracking a few large particles in three different background flows, we demonstrated that the fluid flow velocity can accurately be reconstructed by approximating the particulate phase space and taking the limit $\mathrm{St} \to 0$. This approach is essentially different from approximating the fluid flow velocity by using small, but finite-size particles ($\mathrm{St} \ll 1$) of almost the same St and $\varrho$, as typically done in experimental flow measurements. In fact, combining the trajectories of particles with different St allows to approximate the particle velocity in the hyperspace $(\mathrm{St}, \varrho, ..., \boldsymbol{x})$ and taking the limit $\mathrm{St} \to 0$ allows to get rid of finite-size and inertial effects. Moreover, in the tracer limit, boundary effects vanish ($\lim_{\mathrm{St}\to 0} \boldsymbol{F}_b = 0$) and we can rigorously enforce the fluid flow boundary conditions along the walls, overcoming the usual limitations of experimental particle measurements near the boundaries.

A further advantage of our approach arises when dilute polydisperse suspensions of large particles are considered. In this case, if the particles are tracked for reasons independent of the reconstruction of the background flow, our approach allows to efficiently and accurately retrieve the unperturbed fluid flow without any additional experimental measurement. We stress that assuming that the unperturbed flow velocity is well approximated by the large-particle velocity would not be accurate. Approximating the phase space and taking the asymptotic limit $\mathrm{St} \to 0$ are therefore required steps for an accurate reconstruction of the background flow.

A similar approach can also be employed for two- and four-way coupled simulations, as well as for fully-resolved simulations. In fact, the methodology here proposed does not rely on a specific particle motion model, but only requires that the tracer limit is recovered when $\mathrm{St} \to 0$. Limitations in terms of the particle volume ratio apply.

Moreover, our approach is straightforward to extend to time-dependent flows by including $t$ among the coordinates of the particulate phase space. This method consists only of

instantaneous characterizations of the phase space, and can therefore be used for fluctuating flows by carrying out the phase-space approximation and taking the limit for $\mathrm{St} \to 0$ at each instant of time. Hence, also turbulent flow measurement techniques can benefit from it. When experimental uncertainties are considered, the accuracy of the phase space reconstruction will be affected by them, leading to a worse approximation of the interpolant $\boldsymbol{V}(\mathrm{St}, \varrho, x, y, ...)$ the larger the errorbar in St, $\varrho$, etc. We moreover point out that our approach is more sensitive to errors committed for small-Stokes-number particles since their trajectories are more influential when taking the limit $\mathrm{St} \to 0$. We however stress that the method has been proven robust to the reconstruction of the phase space by means of large particles, which are normally affected by lower relative measurement errors. Finally, our approach can be used for modeling the particle–boundary interaction forces starting from experimental particle tracking: Computing $\tilde{\boldsymbol{u}} = \lim_{\mathrm{St}\to 0} \boldsymbol{V}(\mathrm{St}, \varrho, x, y) \approx \boldsymbol{u}(x, y)$, and measuring $\boldsymbol{v}(t)$ and $\boldsymbol{x}(t)$, one can plug them in (1) to retrieve $\boldsymbol{F}_b$.

### Appendix A: Near-wall shear flow: $\mathbf{Fr}^2 = 10^{-4}$ and $\mathbf{Fr}^2 = 10^{-5}$

The fluid flow reconstruction for Froude number $\mathrm{Fr}^2 = 10^{-4}$ and $\mathrm{Fr}^2 = 10^{-5}$ is reported in fig. 5. Its panels are organized using the same template employed for $\mathrm{Fr}^2 = 10^{-6}$. We stress that changing Fr is not a viable option for experimental measurements since it implies a change of $H$ or $U$. For this reason we treated Fr as a given constant and did not include it among the coordinates of the hyperspace to interpolate, even if the reconstruction of the particulate phase space would benefit from using Fr as a variable.


[1] R. M. Iverson, M. E. Reid, and R. G. LaHusen, "Debris-flow mobilization from landslides," Ann. Rev. Earth Planet. Sci. **25**, 85–138 (1997).

[2] A. R. Minerick, A. E. Ostafin, and H. C. Chang, "Electrokinetic transport of red blood cells in microcapillaries," Electrophoresis **23**, 2165–2173 (2002).

[3] W. C. Hinds, *Aerosol technology: properties, behavior, and measurement of airborne particles* (John Wiley & Sons, 2012).

[4] H. Burtscher, S. Künzel, and C. Hüglin, "Characterization of particles in combustion engine exhaust," J. Aerosol Sci. **29**, 389–396 (1998).

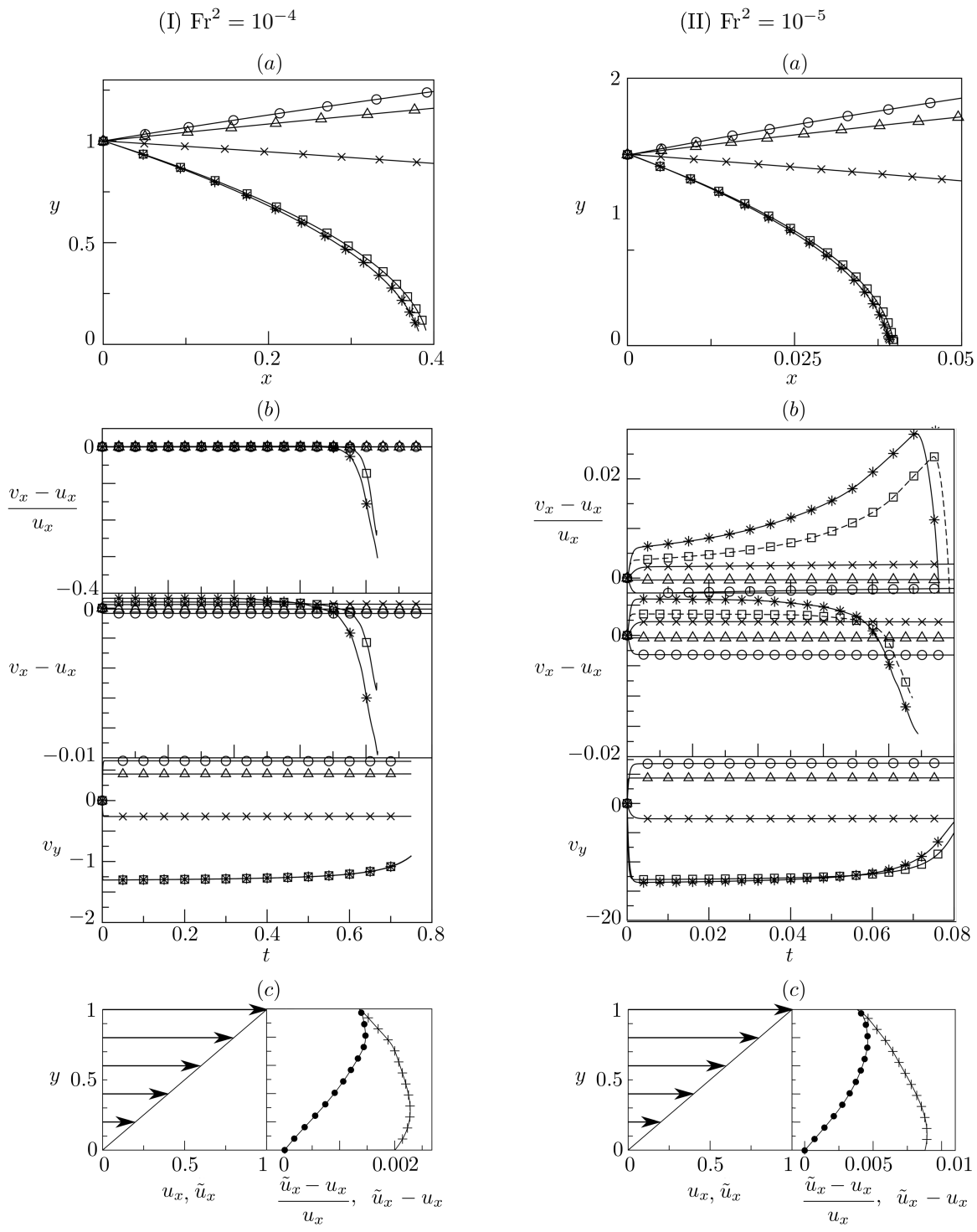


FIG. 5. (a) Particle trajectories. (b) Deviation of the particle velocity from the fluid flow velocity. (c) Fluid velocity $u_x$ (arrows), approximation of the fluid flow $\tilde{u}_x$ (solid line), relative (+) and absolute (•) approximation error (right panel) for the horizontal velocity. In (a) and (b), the markers depict: $(a, \varrho) = (0.02, 0.5)$, ∘, $(0.02, 2.5)$, □, $(0.03, 1.7)$, ∗, $(0.04, 0.8)$, △, and $(0.05, 1.05)$, ×. (I) refers to $\mathrm{Fr}^2 = 10^{-4}$, whereas (II) depicts results for $\mathrm{Fr}^2 = 10^{-5}$.

[5] D. Schwabe, A. I. Mizev, M. Udhayasankar, and S. Tanaka, "Formation of dynamic particle accumulation structures in oscillatory thermocapillary flow in liquid bridges," Phys. Fluids **19**, 072102 (2007).

[6] F. Romanò, H. Wu, and H. C. Kuhlmann, "A generic mechanism for finite-size coherent particle structures," Int. J. Multiphase Flow **111**, 42–52 (2019).

[7] S. T. Wereley and C. D. Meinhart, "Recent advances in micro-particle image velocimetry," Ann. Rev. Fluid Mech. **42**, 557–576 (2010).

[8] K. Nishino, N. Kasagi, and M. Hirata, "Three-dimensional particle tracking velocimetry based on automated digital image processing," J. Fluids Eng. **111**, 384–391 (1989).

[9] C. Kuehn, F. Romanò, and H. C. Kuhlmann, "Tracking particles in flows near invariant manifolds via balance functions," Nonlinear Dyn. **92**, 983–1000 (2018).

[10] F. Romanò, H. C. Kuhlmann, M. Ishimura, and I. Ueno, "Limit cycles for the motion of finite-size particles in axisymmetric thermocapillary flows in liquid bridges," Phys. Fluids **29**, 093303 (2017).

[11] J. C. Lasheras and K.-K. Tio, "Dynamics of a small spherical particle in steady two-dimensional vortex flows," Appl. Mech. Rev. **47**, S61–S69 (1994).

[12] F. Romanò and H. C. Kuhlmann, "Particle-boundary interaction in a shear-driven cavity flow," Theor. Comput. Fluid Dyn. **31**, 427–445 (2017).

[13] K. Bajer, "Hamiltonian formulation of the equations of streamlines in three-dimensional steady flows," Chaos, Solitons & Fractals **4**, 895–911 (1994).

[14] J. Bec, L. Biferale, G. Boffetta, A. Celani, M. Cencini, A. Lanotte, S. Musacchio, and F. Toschi, "Acceleration statistics of heavy particles in turbulence," J. Fluid Mech. **550**, 349–358 (2006).

[15] F. Toschi and E. Bodenschatz, "Lagrangian properties of particles in turbulence," Ann. Rev. Fluid Mech. **41**, 375–404 (2009).

[16] J. Bec, L. Biferale, G. Boffetta, M. Cencini, S. Musacchio, and F. Toschi, "Lyapunov exponents of heavy particles in turbulence," Phys. Fluids **18**, 091702 (2006).

[17] M. R. Maxey and J. J. Riley, "Equation of motion for a small rigid sphere in a nonuniform flow," Phys. Fluids **26**, 883–889 (1983).

[18] G. A. Voth, A. La Porta, A. M. Crawford, J. Alexander, and E. Bodenschatz, "Measurement of particle accelerations in fully developed turbulence," J. Fluid Mech. **469**, 121–160 (2002).

[19] N. M. Qureshi, M. Bourgoin, C. Baudet, A. Cartellier, and Y. Gagne, "Turbulent transport of material particles: an experimental study of finite size effects," Phys. Rev. Lett. **99**, 184502 (2007).

[20] H. Xu and E. Bodenschatz, "Motion of inertial particles with size larger than kolmogorov scale in turbulent flows," Physica D: Nonlinear Phenomena **237**, 2095–2100 (2008).

[21] R. Volk, E. Calzavarini, E. Leveque, and J.-F. Pinton, "Dynamics of inertial particles in a turbulent von kármán flow," J. Fluid Mech. **668**, 223–235 (2011).

[22] R. Zimmermann, Y. Gasteuil, M. Bourgoin, R. Volk, A. Pumir, and J.-F. Pinton, "Rotational intermittency and turbulence induced lift experienced by large particles in a turbulent flow," Phys. Rev. Lett. **106**, 154501 (2011).

[23] G. Falkovich, H. Xu, A. Pumir, E. Bodenschatz, L. Biferale, G. Boffetta, A. S. Lanotte, and F. Toschi, "On lagrangian single-particle statistics," Phys. Fluids **24**, 055102 (2012).

[24] L. Botto and A. Prosperetti, "A fully resolved numerical simulation of turbulent flow past one or several spherical particles," Phys. Fluids **24**, 013303 (2012).

[25] M. Cisse, H. Homann, and J. Bec, "Slipping motion of large neutrally buoyant particles in turbulence," J. Fluid Mech. **735** (2013).

[26] P. J. Ireland and O. Desjardins, "Improving particle drag predictions in euler–lagrange simulations with two-way coupling," J. Comput. Phys. **338**, 405–430 (2017).

[27] J. A. K. Horwitz and A. Mani, "Accurate calculation of stokes drag for point–particle tracking in two-way coupled flows," J. Comput. Phys. **318**, 85–109 (2016).

[28] T. Fukada, S. Takeuchi, and T. Kajishima, "Self-induced velocity correction for improved drag estimation in euler–lagrange point-particle simulations," Int. J. Multiphase Flow **113**, 165–178 (2019).

[29] S. Balachandar, K. Liu, and M. Lakhote, "Self-induced velocity correction for improved drag estimation in euler–lagrange point-particle simulations," J. Comput. Phys. **376**, 160–185 (2019).

[30] S. Balachandar and J. K. Eaton, "Turbulent dispersed multiphase flow," Ann. Rev. Fluid Mech. **42**, 111–133 (2010).

[31] F. Romanò and H. C. Kuhlmann, "Finite-size Lagrangian coherent structures in thermocapillary liquid bridges," Phys. Rev. Fluids **3**, 094302 (2018).

[32] F. Romanò, P. Kunchi Kannan, and H. C. Kuhlmann, "Finite-size Lagrangian coherent structures in a two-sided lid-driven cavity," Phys. Rev. Fluids **4**, 024302 (2019).

[33] E. Calzavarini, R. Volk, M. Bourgoin, E. Lévêque, J.-F. Pinton, and F. Toschi, "Acceleration statistics of finite-sized particles in turbulent flow: the role of faxén forces," J. Fluid Mech. **630**, 179–189 (2009).

[34] K. Gustavsson and B. Mehlig, "Distribution of relative velocities in turbulent aerosols," Physical Review E **84**, 045304 (2011).

[35] H. Faxén, "Der Widerstand gegen die Bewegung einer starren Kugel in einer zähen Flüssigkeit, die zwischen zwei parallelen ebenen Wänden eingeschlossen ist," Ann. Phys. **373**, 89–119 (1922).

[36] H. Brenner, "The slow motion of a sphere through a viscous fluid towards a plane surface," Chem. Eng. Sci. **16**, 242–251 (1961).

[37] A.J. Goldman, R.G. Cox, and H. Brenner, "Slow viscous motion of a sphere parallel to a plane wall: Ii couette flow," Chem. Eng. Sci. **22**, 653–660 (1967).

[38] A.J. Goldman, R.G. Cox, and H. Brenner, "Slow viscous motion of a sphere parallel to a plane wall: I motion through a quiescent fluid," Chem. Eng. Sci. **22**, 637–651 (1967).

[39] F. Romanò, "Oscillatory switching centrifugation: dynamics of a particle in a pulsating vortex," J. Fluid Mech. **857**, R3 (2018).